Escola de Camins
Escola Tècnica Superior d'Enginyeria de Camins, Canals i Ports
UPC BARCELONA**TECH**

MASTER THESIS

Master

Màster en Enginyeria de Camins, Canals i Ports

Title

Real-time monitoring of temperature applied to the Automated Tape Placement (ATP) composite manufacturing process

Author

Joel Torres Serra

Tutor

Antonio Huerta Cerezuela
José-Vicente Aguado López

Speciality

Especialiat en enginyeria computacional

Date

July 4th, 2014

Abstract

In this master thesis numerical simulation is applied to monitoring of temperature evolution in the conformation of thermoplastic laminated structures by the Automated Tape Placement industrial process in real-time, which nowadays constitutes a challenging issue. The objective of this work is to assess the behavior of enhanced models of the transient heat problem in study by analyzing the influence of thermal properties to the overall behavior of the solution.

A recently introduced methodology is presented which allows performance of real-time temperature monitoring in two stages. First, a generalized transfer function associated to the problem in study is solved and thus a virtual chart of multi-parametric solutions can be generated thanks to the use of the Proper Generalized Decomposition technique. Second, the obtained solution is particularized and fast integration of temperature field can be carried out so that real-time control of the process is enabled.

Two examples of practical application of the proposed methodology are conducted. On one hand, parametric analysis of the problem including anisotropic thermal conductivity as extra-coordinate of the solution is carried out. The impact of the ratio of principal thermal conductivities on the behavior and accuracy of the solution is observed. On the other hand, a problem including an interface subject to contact thermal conductance is considered. Also, the influence of variability of this parameter is studied. In both cases, verification of the obtained results is made against reference solutions based on the finite element method.

In conclusion, results show that accuracy of the obtained solutions is strongly related to the order of magnitude of values included in the ranges of considered extra-coordinates when building up computational vademecums for application in real industrial problems. Therefore, the scale of studied problems needs to be validated with experimental data beforehand so that decision making operations can be based on reliable real-time monitoring numerical simulations.

Contents

List of figures

Chapter 1

Introduction

The Automated Tape Placement (ATP) [1, 2] is a high speed manufacturing method intended for the production of advanced thermoplastic composites, laminated composite structures with thermoplastic polymeric matrix. The ATP is attractive to the industry as it is a fast, clean and automated process, despite being a challenging issue.

In the ATP industrial process, as depicted in Figure 1.1, a tape is fed into a placement head and heated along with the substrate, consisting in the previously welded tapes, as it approaches a consolidation device. The tape and the substrate are pushed together as pressure is in turn applied to the interface being joined and thus forming a bond. ATP uses a diode laser as the heat source because of its ability to deliver more heating power, as well as having a near instantaneous response, rather than other systems based on hot gas torches. A cylindrical consolidation roller is used as the consolidation device, to ensure the required conditions for appropriate welding.

The power and trajectory of the laser, which are important factors of the temperature field, strongly affect the quality of thermoplastic composites obtained by the ATP. Combinations of these two parameters must be carried out off-line so that the thermal distribution is verified in the part, considering that during the production process feedback control systems are not applicable unless the temperature field is known in real-time. Moreover, records of temperature information captured by thermocouples can be used for a posteriori quality control purposes.

The modeling and optimization of ATP by numerical simulation turns out to be the preferable choice, compared to the use of experimental methods, in order to assess

Figure 1.1   Diagram showing the ATP process [2]

the associated thermo-mechanical problem. Particularly, the real-time monitoring of the temperature field from in situ measurements might allow real-time decision making strategies, as well as feedback control systems command. The so-called Proper Generalized Decomposition (PGD) model order reduction methodology [3] –based on the use of a separated representation of the unknown thermal field– is considered to be suitable for building a parameterized solution to address this issue, having recently been proven [4] that reciprocity holds in a space-frequency framework of the thermal problem and thus an approach based on generalized transfer functions is feasible.

This master thesis aims to apply the aforementioned numerical method to a real industrial problem. The ATP thermal model is developed by introducing anisotropic conductivity and contact thermal resistance into it and simulated using the proposed technique. Verification of the resulting work is conducted against standard simulations and both the error and computational time are analyzed and compared as well.

Chapter 2

The ATP thermal model

The study of heat transfer involved in the Automated Tape Placement industrial process is crucial to improve this technology. Large thermal gradients are experienced during the successive heating and cooling of the structures built by the ATP, contributing to the development of residual stresses in their conformation. Moreover, the distinct thermal proprieties of the fiber and matrix of thermoplastic composites –the large differences in the respective thermal coefficients– cause important deformation at the matrix-fiber interface. Furthermore, stresses are also induced by consecutive plies not having the same reinforcement orientations. Consequently, notable effects on the mechanical properties and geometry of the resultant plate or shell, such as inter-ply delamination, matrix cracking and distortion, are due to springback to which residual stresses are relevant to and which accurate thermal monitoring can prevent.

The simulation of the ATP manufacturing process is based on some assumptions with respect to the associated thermal model. First, unlike for the actual in situ process, a coordinate system attached to a two-dimensional plate-like domain is considered, since materials with in-plane unidirectional thermal properties are used in practice, without loss of generality. Consequently, boundary conditions become time dependent; hence the line speed of the placement head, which in principle moves with a constant velocity, is implicitly introduced into the heating source. The compatibility of this approach is studied in [1], where the relation between temperature in moving and fixed unidirectional frames –imposing fixed temperature values on both ends of a thin tape, as well as null heat flux– is evaluated, as shown in Figure 2.1. Furthermore, the incoming tow is assumed instantaneously laid down along the substrate, regarding geometry simplification
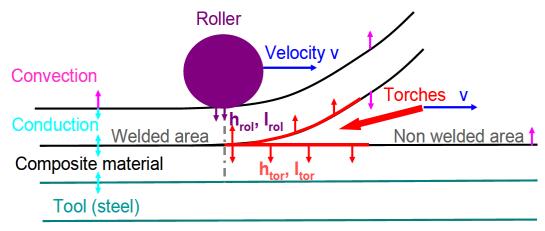
Figure 2.1   Scheme of the process modeling [5]

purposes. Therefore, the heating device is assumed moving on the upper free surface.

The bonding of two thermoplastic layers demands certain physical conditions: on one hand, intimate contact, a measure of the degree of physical contact between the two surfaces being pushed together, governed by the initial geometry of the tapes, temperature and pressure; on the other hand, autohesion, the diffusion of polymer molecules across the interface. The low conductivity of thermoplastics allows local heating to provide the interface with adequate temperature. Therefore, temperature has to be controlled so it is high enough to ensure the interdiffusion of macromolecules, for a time large enough in so far as significant material degradation is prevented. The coupling of the thermal model with the crystallization kinetics is regarded in [5], besides molecular diffusion and material degradation. Hereafter, the effects related to changes of phase, such as solidification or crystallization, are neglected as well as the involved inelastic behaviors. After the heat source is applied, the incoming layer adheres to the substrate considering thermal contact conductance at the inter-plies, with bonding depending on the heat exchange through the interface.

The initial conditions of the ATP thermal model consist of both the substrate and the incoming tape having the ambient temperature. When it comes to boundary conditions, convection is enforced on the upper surface, except in the region where the heating source applies; conduction transmission conditions can be imposed on the contacts at the inter-plies, as already stated, and also at the roller-composite or
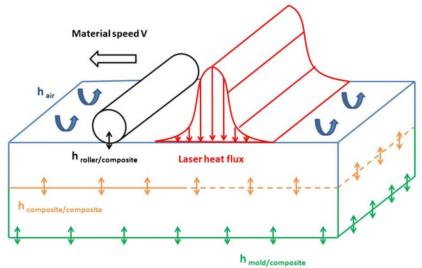
Figure 2.2   ATP thermal model [1]

at the composite-work-plane interfaces, as shown in Figure 2.2, even though the last two cases are not considered, and null heat flux is there enforced instead.

In view of the above, in the space-time domain, the solution to the general transient heat transfer model problem attached to ATP can be defined as the temperature response, $u(\mathbf{x}, t)$, for a material domain $\Omega \subset \mathbb{R}^2$ with boundary $\partial\Omega$, partitioned into a Robin frontier, Γ_R, corresponding to the heat flux inflow surface, and two Neumann frontiers, Γ_N^{in} which corresponds to the interior inter-ply contact interface and Γ_N^{ex} for the rest of the exterior contour, such that $\overline{\partial\Omega} = \overline{\Gamma_R} \cup \overline{\Gamma_N^{in}} \cup \overline{\Gamma_N^{ex}}$, $\Gamma_R \cap \Gamma_N^{in} \cap \Gamma_N^{ex} = \{\emptyset\}$ and for a time interval $I_t = (0, T]$, under an external arbitrary transient excitation $q(\mathbf{x}, t), \forall (\mathbf{x}, t) \in \Gamma_R \times I_t$:

$$
\begin{cases}
m\dfrac{\partial u}{\partial t} - \boldsymbol{\nabla} \cdot (\boldsymbol{K} \cdot \boldsymbol{\nabla}u) & = & 0 & in\ \Omega \times I_t \\
\boldsymbol{n} \cdot (\boldsymbol{K} \cdot \boldsymbol{\nabla}u) & = & q - l(u - u_\infty) & on\ \Gamma_R \times I_t \\
\boldsymbol{n} \cdot (\boldsymbol{K} \cdot \boldsymbol{\nabla}u) & = & -c\Delta u & on\ \Gamma_N^{in} \times I_t \\
\boldsymbol{n} \cdot (\boldsymbol{K} \cdot \boldsymbol{\nabla}u) & = & 0 & on\ \Gamma_N^{ex} \times I_t \\
u & = & u_\infty & on\ \Omega \times \{0\}
\end{cases}
\qquad (\,2.1\,)
$$

where $m\left[\dfrac{J}{m^3 \cdot K}\right]$ is the volumetric heat capacity, $\boldsymbol{K}\left[\dfrac{W}{m \cdot K}\right]$ is the thermal conductivity matrix, $\boldsymbol{n}$ is the exterior unit normal to the boundaries, $l\left[\dfrac{W}{m^2 \cdot K}\right]$ is the heat transfer coefficient, u_∞ is the external ambient temperature, $c\left[\dfrac{W}{m^2 \cdot K}\right]$ is the thermal contact conductance and Δu is the temperature drop across the interface.

Chapter 3

Real-time monitoring

Real-time temperature monitoring of the ATP process is mandatory to define suitable feedback control systems. A thermopair typically placed on the composite-placement head interface of the domain of interest can provide the temperature history, the post-processing of which allows for an appropriate assessment of the running process. Herein, the approach proposed by Aguado et al. [4] is presented. The objective is to apply this fast simulation methodology to find a computable representation of $u(\mathbf{x}_0, t_0)$, the temperature at an arbitrary boundary point $\mathbf{x}_0 \in \Gamma_N^{ex}$ at any instant $t_0 \in I_t$, that is a solution of the thermal model in equation (2.1).

The key point of the simulation strategy is the feasibility of the application of the reciprocity principle to the governing equation of the problem. For this reason, a space-time approach is initially precluded since the heat equation operator is not self-adjoint in this domain. Harmonic analysis is considered as the basis of an alternative procedure, where the forward and inverse Fourier transforms (3.1) of temperature are used:

$$
\begin{cases}
\hat{u}(\mathbf{x}, \omega) = \mathcal{F}[u(\mathbf{x}, t)] = \displaystyle\int_{-\infty}^{\infty} u(\mathbf{x}, t) e^{-i\omega t} \, dt \\[2em]
u(\mathbf{x}, t) = \mathcal{F}^{-1}[\hat{u}(\mathbf{x}, \omega)] = \dfrac{1}{2\pi} \displaystyle\int_{-\infty}^{\infty} \hat{u}(\mathbf{x}, \omega) e^{i\omega t} \, d\omega
\end{cases}
\tag{3.1}
$$

where ω is the angular frequency and i denotes the imaginary unit. Harmonic solutions are related to long-term responses and so they do not rely on the initial conditions of problems. However, for practical purposes, transient regime effects become negligible as the obtained long-term solution is rapidly met. Then, recalling the properties of Fourier transform [6], problem (2.1) can be rewritten as:

$$
\begin{cases}
im\omega\hat{u} - \boldsymbol{\nabla}\cdot(\boldsymbol{K}\cdot\boldsymbol{\nabla}\hat{u}) &= \ 0 & in\ \Omega \\
\boldsymbol{n}\cdot(\boldsymbol{K}\cdot\boldsymbol{\nabla}\hat{u}) &= \ \hat{q} - l\hat{u} & on\ \Gamma_R \\
\boldsymbol{n}\cdot(\boldsymbol{K}\cdot\boldsymbol{\nabla}\hat{u}) &= \ -c\Delta\hat{u} & on\ \Gamma_N^{in} \\
\boldsymbol{n}\cdot(\boldsymbol{K}\cdot\boldsymbol{\nabla}\hat{u}) &= \ 0 & on\ \Gamma_N^{ex}
\end{cases}
\tag{3.2}
$$

where the external ambient temperature u_∞ is omitted as it is regarded to be constant in time and thus it can be afterwards added to the obtained solution. The equivalent weak formulation of (3.2) reads:

Find $\hat{u} \in H^1(\Omega)$ such that
$$(im\omega\hat{u},\hat{v})_\Omega + (\boldsymbol{K}\cdot\boldsymbol{\nabla}\hat{u},\boldsymbol{\nabla}\hat{v})_\Omega + \langle l\hat{u},\hat{v}\rangle_{\Gamma_R} + \langle c\Delta\hat{u},\hat{v}\rangle_{\Gamma_N^{in}} = \langle\hat{q},\hat{v}\rangle_{\Gamma_R} \tag{3.3}$$
for all test function $\hat{v} \in H^1(\Omega)$

where

$$(f,g)_\Omega = \int_\Omega f\cdot g^*\,d\Omega \quad ; \quad \langle f,g\rangle_\Gamma = \int_\Gamma f\cdot g^*\,d\Gamma \tag{3.4}$$

indicate the scalar product of two complex functions, f and g, in the general case, in the space domain of the problem, $(f,g)_\Omega$, and the trace over the different parts of its boundary, $\langle f,g\rangle_\Gamma$. Also, f^* denotes the complex conjugate of a generic complex-valued function, f. Hence, the differential operator associated to equation (3.3) turns out to be symmetrical, yet not hermitian –that is, the system matrix associated to a finite-dimensional basis of the space of solutions is equal to its transpose although it is not equal to its conjugate transpose– and so reciprocity principle is proven to hold for the case of real harmonic excitations, as follows. Suppose that a real arbitrary excitation $\hat{q}_1(\mathbf{x},\omega) \in \mathbb{R}$ produces a thermal field $\hat{u}_1(\mathbf{x},\omega) \in \mathbb{C}$ that is solution of (3.2) for a given frequency. Suppose that another real arbitrary heat flux $\hat{q}_2(\mathbf{x},\omega) \in \mathbb{R}$ which analogously produces field $\hat{u}_2(\mathbf{x},\omega) \in \mathbb{C}$ at the same angular frequency. Then, reciprocity is satisfied since the following is true:

$$\int_{\Gamma_R}\hat{q}_1\hat{u}_2^*\,d\Gamma = \int_{\Gamma_R}\hat{q}_2\hat{u}_1^*\,d\Gamma \tag{3.5}$$

Moreover, taking into account elements of harmonic analysis, the decomposition of a real arbitrary external excitation into the sum of its corresponding even $q_e(\mathbf{x},t) \in \mathbb{R}$ and odd $q_o(\mathbf{x},t) \in \mathbb{R}$ counterparts such that $q(\mathbf{x},t) = q_e(\mathbf{x},t) + q_o(\mathbf{x},t) \in \mathbb{R}$, allows for the decomposition of the original space-time domain problem into two identical problems in the space-frequency domain based on the

corresponding real even $\hat{q}_e(\mathbf{x}, \omega) \in \mathbb{R}$ and odd $\hat{q}_o(\mathbf{x}, \omega) \in \mathbb{R}$ counterparts of the heat source such that $\hat{q} = \hat{q}_e + i\hat{q}_o \in \mathbb{C}$. The solution of (3.2) for these two real excitations accords with the real and imaginary parts of the solution of temperature response at any point of the space domain for any given frequency value such that $\hat{u}(\mathbf{x}_0, \omega) = \hat{u}_e(\mathbf{x}_0, \omega) + i\hat{u}_o(\mathbf{x}_0, \omega) \in \mathbb{C}$.

Due to all of this, the generalized transfer function, $\hat{h}(\mathbf{x}, \omega)$, is defined as the solution of the following expression:

$$\begin{cases} im\omega\hat{h} - \nabla \cdot (\mathbf{K} \cdot \nabla\hat{h}) &= 0 & in\ \Omega \\ \mathbf{n} \cdot (\mathbf{K} \cdot \nabla\hat{h}) &= \delta(\mathbf{x} - \mathbf{x}_0) - l\hat{h} & on\ \Gamma_R \\ \mathbf{n} \cdot (\mathbf{K} \cdot \nabla\hat{h}) &= -c\Delta\hat{h} & on\ \Gamma_N^{in} \\ \mathbf{n} \cdot (\mathbf{K} \cdot \nabla\hat{h}) &= 0 & on\ \Gamma_N^{ex} \end{cases} \qquad (3.6)$$

for each frequency $\omega \in I_\omega \subseteq \mathbb{R}$ within the range of feasible values and where $\delta(\mathbf{x} - \mathbf{x}_0)$ denotes a Dirac delta flux imposed at the monitoring point $\mathbf{x}_0$. Because of only real excitations being regarded, reciprocity can be applied resulting in:

$$\hat{u}(\mathbf{x}_0, \omega) = \langle\hat{h}, \hat{q}_e\rangle_{\Gamma_R} + i\langle\hat{h}, \hat{q}_o\rangle_{\Gamma_R} = \int_{\Gamma_R} \hat{h}(\mathbf{x}, \omega)\hat{q}(\mathbf{x}, \omega)\, d\Gamma = \langle\hat{h}, \hat{q}^*\rangle_{\Gamma_R} \qquad (3.7)$$

It is noted that temperature is not the straight forward scalar product of the generalized transfer function of the problem over a specific external excitation, but over its complex conjugate instead, which is because the related differential operator is not hermitian in the space-frequency domain. Applying the inverse Fourier transform and the convolution theorem to equation (3.7), the space-frequency domain monitoring is turned into a space-time domain representation of temperature at the desired point boundary point $\mathbf{x}_0 \in \Gamma_N^{ex}$ at any instant $t_0 \in I_t$ by equation (3.8):

$$u(\mathbf{x}_0, t_0) = \int_0^{t_0} \langle h(\mathbf{x}, \tau), q(\mathbf{x}, t_0 - \tau)\rangle_{\Gamma_R}\, d\tau \qquad (3.8)$$

where the scalar product notation is consistent owing to the external excitation being described by a real function.

Therefore, on one hand, the obtained solution of $u(\mathbf{x}_0, t_0)$ only requires knowledge of the arbitrary external imposed excitation q up to the monitored instant t_0. On the other hand, the solution of the generalized transfer function $\hat{h}$ is needed to be

determined for all angular frequencies belonging to the interval I_ω prescribed by the forced external excitation, which must be known a priori in order to calculate the inverse Fourier transform of $\hat{h}$, what in principle complicates the practical use of this methodology. Nevertheless, the use of separated representation techniques allow finding the solution of equation (3.6) for the predefined range of frequencies which can be done once and off-line using the Proper Generalized Decomposition reduced order method, as described further on. In this way, the response at the monitoring point of interest can be recovered performing a computationally inexpensive on-line post-processing step, allowing for real-time control of the Automated Tape Placement process.

Finally, it is important to notice that space-frequency domain representations are broadly used in engineering, for instance, in dynamics of structures. In this framework, numerical analysis of structures subjected to dynamic excitations generally integrates finite element approaches into discrete harmonic analysis based strategies, like the one presented above, in order to obtain the system response far enough from the initial transient regime. An exhaustive review of the space-frequency domain method of response analysis in addition to the discrete Fourier transform methods in the context of structural dynamics is presented in [7].

Chapter 4

The Proper Generalized Decomposition

Real-time monitoring of ATP has been established in Chapter 3, for which reason the generalized transfer function of the problem has been defined. Numerical simulation based on the proposed approach can be carried out within procedures of on-line control of the system under study making use of parametric Proper Generalized Decomposition based vademecums [8], calculated once beforehand in off-line stages. The numerical model is enriched through the use of PGD-based solutions as parameters can be regarded as extra-coordinates. Then, the computation of the generalized transfer function associated to the problem of study by a PGD separated representation of the unknown field [9, 10], as illustrated in the following, becomes of interest for the application of the presented real-time monitoring scheme.

4.1   Illustrative example

Consider a generalized transfer function, $\hat{h}(\mathbf{x}, \omega)$, in a predefined range of angular frequencies I_ω, satisfying:

$$\begin{cases} i\omega\hat{h} - \mathbf{\nabla}^2\hat{h} & = & 0 & in\ \Omega \times I_\omega \\ \boldsymbol{n} \cdot \mathbf{\nabla}\hat{h} & = & \delta(\mathbf{x} - \mathbf{x}_0) & on\ \Gamma_N \times I_\omega \\ \boldsymbol{n} \cdot \mathbf{\nabla}\hat{h} & = & 0 & on\ \partial\Omega/\Gamma_N \times I_\omega \end{cases} \qquad (\,4.1\,)$$

All thermal parameters have been disregarded, without loss of generality, as well as convection and contact conductance heat exchange terms have not been considered, with respect to expression of the full generalized transfer function in (3.6). The weak formulation of (4.1) yields:

Find $\hat{h}(\boldsymbol{x}, \omega)$ such that

$$\int_{I_\omega} \left(i\omega\hat{h}, \hat{v}\right)_\Omega \, d\omega + \int_{I_\omega} \left(\boldsymbol{\nabla}\hat{h}, \boldsymbol{\nabla}\hat{v}\right)_\Omega \, d\omega = \int_{I_\omega} \hat{v}^*(\mathbf{x}_0, \omega) \, d\omega \tag{4.2}$$

for all test function $\hat{v}(\boldsymbol{x}, \omega)$ in an appropriate functional space.

The aim of the separated representation method is to compute n couples of functions $\left\{\left(X_j(\mathbf{x}), W_j(\omega)\right)\right\}_{j=1}^{j=n}$ such that $\{X_j\}_{j=1}^{j=n} \in H^1(\Omega)$ and $\{W_j\}_{j=1}^{j=n} \in L^2(I_\omega)$ leading to an approximated solution of $\hat{h}$ in the separable form:

$$\hat{h}(\mathbf{x}, \omega) \approx \hat{h}^n(\mathbf{x}, \omega) = \sum_{j=1}^{n} X_j(\mathbf{x}) \cdot W_j(\omega) \tag{4.3}$$

Hence, a nonlinear problem must be solved in order to determine each new term of the approximation. The construction of $\hat{h}^n$ is performed by application of the so-called alternating directions fixed point algorithm. In this progressive scheme, the first $0 \leq m < n$ functional couples involved in (4.3) are supposed known and each iteration step is intended for an enrichment couple $\left(R(\mathbf{x}), S(\omega)\right)$ to constitute the next functional couple (X_{m+1}, W_{m+1}) after convergence of the fixed point algorithm:

$$\hat{h}^{m+1}(\mathbf{x}, \omega) = \hat{h}^m(\mathbf{x}, \omega) + R(\mathbf{x}) \cdot S(\omega) \tag{4.4}$$

To start building up the solution, the test function $\hat{v}$ is assumed as:

$$\hat{v}(\mathbf{x}, \omega) = \hat{v}_R(\mathbf{x}) \cdot S(\omega) + R(\mathbf{x}) \cdot \hat{v}_S(\omega) \tag{4.5}$$

with variations $\hat{v}_R(\mathbf{x}) \in H^1(\Omega)$ and $\hat{v}_S(\omega) \in L^2(I_\omega)$. Introducing (4.4) and (4.5) into (4.2) results in:

$$\int_{\Omega \times I_\omega} (iR \cdot \omega S - \boldsymbol{\nabla}^2 R \cdot S) \cdot (\hat{v}_R \cdot S + R \cdot \hat{v}_S)^* \, d\mathbf{x} \, d\omega$$

$$= \int_{\Omega \times I_\omega} \left(\delta(\mathbf{x} - \mathbf{x}_0) - \hat{h}^m(\mathbf{x}, \omega)\right) \cdot (\hat{v}_R \cdot S + R \cdot \hat{v}_S)^* \, d\mathbf{x} \, d\omega \tag{4.6}$$

The alternating directions fixed point algorithm is applied to compute the couple of functions (R, S) in two stages in each iteration step:

- *Update of $R(\mathbf{x}) \in H^1(\Omega)$*
  $S(\omega)$ is assumed known, which implies that $\hat{v}_S(\omega)$ vanishes in (4.5). Thus, equation (4.6) can be rewritten as:

$$\alpha_S (iR, \hat{v}_R)_\Omega + \beta_S (\boldsymbol{\nabla} R, \boldsymbol{\nabla} \hat{v}_R)_\Omega$$
$$= \gamma_S \hat{v}_R^*(\mathbf{x}_0) - \sum_{j=1}^{m-1} \left[\alpha_S^j (iX_j, \hat{v}_R)_\Omega + \beta_S^j (\boldsymbol{\nabla} X_j, \boldsymbol{\nabla} \hat{v}_R)_\Omega \right] \qquad (4.7)$$

  for all $\hat{v}_R(\mathbf{x}) \in H^1(\Omega)$, with coefficients:

$$\begin{cases} \alpha_S = (\omega S, S)_{I_\omega} \\ \alpha_S^j = (\omega W_j, S)_{I_\omega} \\ \beta_S = (S, S)_{I_\omega} \\ \beta_S^j = (W_j, S)_{I_\omega} \\ \gamma_S = (1, S)_{I_\omega} \end{cases} \qquad (4.8)$$

  which have to be recomputed for every update of S after each iteration. The recovered strong formulation as a system of linear equations can be solved by standard discretization techniques applied to the spatial domain in order to compute the space function R.

- *Update of $S(\omega) \in L^2(I_\omega)$*
  $R(\mathbf{x})$ is already known from the previous stage. Consequently, $\hat{v}$ writes $R(\mathbf{x}) \cdot \hat{v}_S(\omega)$ and equation (4.6) can be rewritten as:

$$\alpha_R (\omega S, \hat{v}_S)_{I_\omega} + \beta_R (S, \hat{v}_S)_{I_\omega}$$
$$= \gamma_R (1, \hat{v}_S)_{I_\omega} - \sum_{j=1}^{m-1} \left[\alpha_R^j (\omega W_j, \hat{v}_S)_{I_\omega} + \beta_R^j (W_j, \hat{v}_S)_{I_\omega} \right] \qquad (4.9)$$

  for all $\hat{v}_S(\mathbf{x}) \in L^2(I_\omega)$, with coefficients:

$$\begin{cases} \alpha_R = (iR, R)_\Omega \\ \alpha_R^j = (iX_j, R)_\Omega \\ \beta_R = (\boldsymbol{\nabla} R, \boldsymbol{\nabla} R)_\Omega \\ \beta_R^j = (\boldsymbol{\nabla} X_j, \boldsymbol{\nabla} R)_\Omega \\ \gamma_R = R(\mathbf{x}_0) \end{cases} \qquad (4.10)$$

  which have to be computed in every iteration from known updates of R. The recovered strong formulation as a point-wise algebraic equation can be solved again using standard discretization techniques applied to the

angular frequency domain so that a continuous approximation of the frequency function S is obtained.

Equations (4.7) and (4.9) are solved iteratively until reaching convergence, in other words, until both enrichment functions reach a fixed point. Considering two consecutive solutions of the enrichment couple, $\left(R^{(p)}(\mathbf{x}), S^{(p)}(\omega)\right)$ and $\left(R^{(p-1)}(\mathbf{x}), S^{(p-1)}(\omega)\right)$, convergence of the alternating directions algorithm is verified when the following stopping criterion is fulfilled:

$$e = \left\|R^{(p)}(\mathbf{x}) \cdot S^{(p)}(\omega) - R^{(p-1)}(\mathbf{x}) \cdot S^{(p-1)}(\omega)\right\| < \varepsilon_e \qquad (4.11)$$

where ε_e is a small enough tolerance parameter and the l^2-norm applies. In the global iterative procedure, each functional couple is defined after reaching convergence of the enrichment couple:

$$X_{m+1}(\mathbf{x}) = R^{(p_{m+1})}(\mathbf{x}) \quad ; \quad W_{m+1}(\omega) = S^{(p_{m+1})}(\omega) \qquad (4.12)$$

where p_{m+1} is the number of iterations required for solving the non-linear problem corresponding to next functional couple that is being calculated.

The global iterative procedure of enrichment is continued up to the n-th iteration, the convergence of which is verified using the residual of the weak form in (4.2), since the exact solution is generally unknown:

$$E = \frac{\left\|i\omega\hat{h} - \boldsymbol{\nabla}^2\hat{h} - \delta(\mathbf{x} - \mathbf{x}_0)\right\|}{\left\|\delta(\mathbf{x} - \mathbf{x}_0)\right\|} < \varepsilon_E \qquad (4.13)$$

where ε_E is a small enough tolerance parameter. Other error estimators based on the assessment of different quantities of interest may be defined.

The introduction of model parameters as extra coordinates into the PGD-based solution entails the increase of dimensionality of the obtained representation. The solution of $N = \sum_{j=1}^{j=n} p_j$ two-dimensional space problems and also N algebraic frequency systems is involved in the solution of the entire procedure of the above example. Therefore, complexity of the PGD scales linearly with the spatial dimension as the cost related to algebraic problems is negligible in terms of efficiency loss towards an accurate solution, unlike for discretization-based

methods, whose complexity increases exponentially with the number of dimensions.

In view of the above, if the number of extra-coordinates is increased, the superiority of PGD with respect to standard approaches is made clear in relation to computational cost and the use of PGD turns out to be an efficient tool. It is the aim of next Chapter 5 to present a generalization of the described procedure to higher-dimensional models.

4.2   General framework

In this section, a general framework of the Proper Generalized Decomposition is presented [10, 11]. Based on tensor notation, it allows for the treatment of more general high-dimensional models by the PGD. In addition, the practical implementation of the PGD needs for the use of discretization techniques to obtain the representation of all involved functions. The finite element method is a robust standard technique broadly used for such interpolation purposes. Moreover, direct solutions of the ATP thermal model by finite elements yield reference approximations that are useful in order to verify the obtained PGD-based representations, and besides, making use of the same interpolation tools.

Consider the weak formulation of a partial differential equation:

$$a\big(u(\mathbf{x}_1, \dots \mathbf{x}_D), v(\mathbf{x}_1, \dots \mathbf{x}_D)\big) = b\big(v(\mathbf{x}_1, \dots \mathbf{x}_D)\big) \qquad (4.14)$$

with $a(u, v)$ and $b(v)$ respectively bilinear and linear forms defined in a multidimensional domain involving not necessarily one-dimensional coordinates, $\{\mathbf{x}_1, \dots \mathbf{x}_D\}$. The solution of (4.14) can be approximated by:

$$u(\mathbf{x}_1, \dots \mathbf{x}_D) \approx \sum_{j=1}^{N} u(\mathbf{x}_1) \cdot \dots \cdot u(\mathbf{x}_D) \qquad (4.15)$$

with tensor form:

$$U = \sum_{j=1}^{n_u} \bigotimes_{d=1}^{D} \mathbf{U}_d^j \qquad (4.16)$$

The discrete form of (4.14) reads:

$$V^T \mathcal{A} U = V^T \mathcal{B} \tag{4.17}$$

where

$$\mathcal{A} = \sum_{j=1}^{n_A} \bigotimes_{d=1}^{D} \mathbb{A}_d^j \quad ; \quad \mathcal{B} = \sum_{j=1}^{n_B} \bigotimes_{d=1}^{D} \mathbf{B}_d^j \tag{4.18}$$

First approximation is arbitrarily set. Iteratively, the separated representation is updated within an enrichment stage that looks for a set of functions $\{\mathbf{R}_1, \dots \mathbf{R}_D\}$ to enrich the solution:

$$U = \underbrace{\sum_{j=1}^{n_u} \bigotimes_{d=1}^{D} \mathbf{U}_d^j}_{U_u} + \underbrace{\bigotimes_{d=1}^{D} \mathbf{R}_d}_{U_R} \tag{4.19}$$

Then, the alternating directions fixed point algorithm is applied to all functions in U_R. Every $\mathbf{R}_j$ is updated in D steps as the rest of enrichment functions, $\{\mathbf{R}_1, \dots \mathbf{R}_{j-1}, \mathbf{R}_{j+1}, \dots \mathbf{R}_D\}$, are assumed known. Thus, the associated test function reads:

$$V = \mathbf{V}_j \bigotimes_{\substack{d=1 \\ d \neq j}}^{D} \mathbf{R}_d \tag{4.20}$$

The discrete weak form involves:

$$V^T \mathcal{A} U_R = \sum_{k=1}^{n_A} \left(\mathbf{V}_j^T \mathbb{A}_j^k \mathbf{R}_j \prod_{\substack{p=1 \\ p \neq j}}^{D} \mathbf{R}_p^T \mathbb{A}_p^k \mathbf{R}_p \right) = \mathbf{V}_j^T \mathbb{S} \mathbf{R}_j \tag{4.21}$$

$$V^T \mathcal{A} U_u = \sum_{k=1}^{n_A} \sum_{s=1}^{n_u} \left(\mathbf{V}_j^T \mathbb{A}_j^k \mathbf{U}_j^s \prod_{\substack{p=1 \\ p \neq j}}^{D} \mathbf{R}_p^T \mathbb{A}_p^k \mathbf{U}_p^s \right) = \mathbf{V}_j^T \mathbf{G} \tag{4.22}$$

$$V^T \mathcal{B} = \sum_{k=1}^{n_B} \left(\mathbf{V}_j^T \mathbf{B}_j^k \prod_{\substack{p=1 \\ p \neq j}}^{D} \mathbf{R}_p^T \mathbf{B}_p^k \right) = \mathbf{V}_j^T \mathbf{F} \tag{4.23}$$

Each $\boldsymbol{R}_j$ is finally determined by solving a linear system:

$$\mathbb{S} \mathbf{R}_j = \mathbf{F} - \mathbf{G} \tag{4.24}$$

Updating U_R is accomplished through the fulfillment of the stopping criterion defined in (4.11) whose discrete form is:

$$e = \left\| U_R^{(p)} - U_R^{(p-1)} \right\| = \sqrt{U_R^{(p)^T} U_R^{(p)} - 2 \cdot U_R^{(p-1)^T} U_R^{(p)} + U_R^{(p-1)^T} U_R^{(p-1)}} < \varepsilon_e \qquad (4.25)$$

where

$$U_R^T U_R = \prod_{j=1}^{D} \mathbf{R}_j^T \mathbf{R}_j \qquad (4.26)$$

Once each U_R is updated, it is added into U_u and the global enrichment strategy proceeds. The presented scheme converges when $n_u = N$, that is, when the number of enrichment steps provides an accurate enough approximation of the unknown field. Quantification of the approximation can be made through equation (4.13) which in tensor form reads [11]:

$$E = \frac{\| \mathcal{A} U - \mathcal{B} \|}{\| \mathcal{B} \|} = \frac{\sqrt{U^T \mathcal{A}^T \mathcal{A} U - 2 \cdot \mathcal{B}^T \mathcal{A} U + \mathcal{B}^T \mathcal{B}}}{\sqrt{\mathcal{B}^T \mathcal{B}}} < \varepsilon_E \qquad (4.27)$$

where

$$\begin{cases} U^T \mathcal{A}^T \mathcal{A} U &= \displaystyle\sum_{j=1}^{n_u} \sum_{k=1}^{n_A} \sum_{p=1}^{n_A} \sum_{s=1}^{n_u} \prod_{d=1}^{D} \mathbf{U}_d^{j^T} \mathbb{A}_d^{k^T} \mathbb{A}_d^{p} \mathbf{U}_d^{s} \\[2mm] \mathcal{B}^T \mathcal{A} U &= \displaystyle\sum_{j=1}^{n_B} \sum_{k=1}^{n_A} \sum_{p=1}^{n_u} \prod_{d=1}^{D} \mathbf{B}_d^{j^T} \mathbb{A}_d^{k} \mathbf{U}_d^{p} \\[2mm] \mathcal{B}^T \mathcal{B} &= \displaystyle\sum_{j=1}^{n_B} \sum_{k=1}^{n_B} \prod_{d=1}^{D} \mathbf{B}_d^{j^T} \mathbf{B}_d^{k} \end{cases} \qquad (4.28)$$

Calculation of the terms involved in the solution of equation (4.14) can be alternatively approximated using the so-called minimal residual PGD [12], whose associated discrete form reads:

$$V^T \mathcal{A}^T \mathcal{A} U = V^T \mathcal{A}^T \mathcal{B} \qquad (4.29)$$

This alternative methodology is intended to solve problems which are not symmetric, for which convergence of the above described procedure cannot be ensured, although its applicability can be extended to general PGD-based solutions. On one hand, the symmetrized PGD scheme appears to be more robust. However,

on the other hand, convergence becomes slower when compared to the standard approach.

4.3   Computer implementation

Following the example illustrated in section 4.1 Illustrative example, the discrete representation is obtained by a finite element interpolation of functions in the corresponding space and angular frequency domains. According to the definition of the generalized transfer function of study (4.1), space domain functions are complex-valued. Therefore, all spatial modes are decomposed into the corresponding real and imaginary parts. Application of the decomposition to spatial enrichment function $R(\mathbf{x})$ reads:

$$R(\mathbf{x}) = Y(\mathbf{x}) + iZ(\mathbf{x}) \in \mathbb{C} \qquad (4.30)$$

where $Y(\mathbf{x}) \in \mathbb{R}$ and $Z(\mathbf{x}) \in \mathbb{R}$ are the real-valued respectively real and imaginary components of $R(\mathbf{x})$. Discretization of the enrichment functions results[1]:

$$\begin{cases} R(\mathbf{x}) \approx \displaystyle\sum_{j=1}^{n_R} \left(Y_j + iZ_j\right) \cdot N_j(\mathbf{x}) = \mathbf{N_x}^T \cdot \{\mathbf{Y} + i\mathbf{Z}\} = \begin{bmatrix} \mathbf{N_x}^T & \mathbf{0} \\ \mathbf{0} & \mathbf{N_x}^T \end{bmatrix} \begin{Bmatrix} \mathbf{Y} \\ \mathbf{Z} \end{Bmatrix} \\ S(\omega) \approx \displaystyle\sum_{j=1}^{n_S} S_j \cdot N_j(\omega) = \mathbf{N_\omega}^T \mathbf{S} \end{cases} \qquad (4.31)$$

where the nodal descriptions of enrichment space –in terms of $\mathbf{Y}$ and $\mathbf{Z}$, the discrete counterparts of the decomposition– and frequency, $\mathbf{S}$, functions as well as vectors $\mathbf{N_x}$ and $\mathbf{N_\omega}$ contain the shape functions for interpolation over the space domain, Ω, and angular frequency domain, I_ω.

From equations (4.7) and (4.9), the matrices related to the discrete forms are defined:

---

[1] The discrete form of a generic operator, $\mathbb{F}(\boldsymbol{\alpha})$, over a complex-valued vector, $\boldsymbol{\alpha} \in \mathbb{C}^{n_\alpha}$, is in general:

$$\begin{array}{rcl} \mathbb{F}: & \mathbb{C}^{n_\alpha} & \longrightarrow & \mathbb{R}^{n_\alpha} \\ & \boldsymbol{\alpha} & \longrightarrow & \begin{Bmatrix} \mathrm{Re}(\boldsymbol{\beta}) \\ \mathrm{Im}(\boldsymbol{\beta}) \end{Bmatrix} = \begin{bmatrix} \mathbb{F}_{Re}^{Re} & \mathbb{F}_{Im}^{Re} \\ \mathbb{F}_{Re}^{Im} & \mathbb{F}_{Im}^{Im} \end{bmatrix} \begin{Bmatrix} \mathrm{Re}(\boldsymbol{\alpha}) \\ \mathrm{Im}(\boldsymbol{\alpha}) \end{Bmatrix} \end{array}$$

so that $\boldsymbol{\beta} = \mathrm{Re}(\boldsymbol{\beta}) + i\,\mathrm{Im}(\boldsymbol{\beta}) \in \mathbb{C}^{n_\alpha}$

$$\left(i\begin{bmatrix} \mathbf{N_x} & \mathbf{0} \\ \mathbf{0} & \mathbf{N_x} \end{bmatrix}, \begin{bmatrix} \mathbf{N_x} & \mathbf{0} \\ \mathbf{0} & \mathbf{N_x} \end{bmatrix} \right)_\Omega = \int_\Omega i\begin{bmatrix} \mathbf{N_x} & \mathbf{0} \\ \mathbf{0} & \mathbf{N_x} \end{bmatrix} \cdot \begin{bmatrix} \mathbf{N_x^T} & \mathbf{0} \\ \mathbf{0} & \mathbf{N_x^T} \end{bmatrix}^* d\mathbf{x}$$

$$= \int_\Omega \begin{bmatrix} \mathbf{N_x} & \mathbf{0} \\ \mathbf{0} & \mathbf{N_x} \end{bmatrix} \cdot \begin{bmatrix} \mathbf{0} & -\mathbf{N_x} \\ \mathbf{N_x} & \mathbf{0} \end{bmatrix} d\mathbf{x} = \begin{bmatrix} \mathbf{0} & -\mathbb{M}_x \\ \mathbb{M}_x & \mathbf{0} \end{bmatrix}$$

(4.32)

where

$$\mathbb{M}_x = \int_\Omega \mathbf{N_x}\mathbf{N_x^T}\, d\mathbf{x}$$

(4.33)

Moreover:

$$\left(\boldsymbol{\nabla}\begin{bmatrix} \mathbf{N_x} & \mathbf{0} \\ \mathbf{0} & \mathbf{N_x} \end{bmatrix}, \boldsymbol{\nabla}\begin{bmatrix} \mathbf{N_x} & \mathbf{0} \\ \mathbf{0} & \mathbf{N_x} \end{bmatrix} \right)_\Omega = \int_\Omega \boldsymbol{\nabla}\begin{bmatrix} \mathbf{N_x} & \mathbf{0} \\ \mathbf{0} & \mathbf{N_x} \end{bmatrix} \cdot \boldsymbol{\nabla}\begin{bmatrix} \mathbf{N_x^T} & \mathbf{0} \\ \mathbf{0} & \mathbf{N_x^T} \end{bmatrix}^* d\mathbf{x}$$

$$= \int_\Omega \boldsymbol{\nabla}\begin{bmatrix} \mathbf{N_x} & \mathbf{0} \\ \mathbf{0} & \mathbf{N_x} \end{bmatrix} \cdot \boldsymbol{\nabla}\begin{bmatrix} \mathbf{N_x^T} & \mathbf{0} \\ \mathbf{0} & \mathbf{N_x^T} \end{bmatrix} d\mathbf{x} = \begin{bmatrix} \mathbb{K} & \mathbf{0} \\ \mathbf{0} & \mathbb{K} \end{bmatrix}$$

(4.34)

where

$$\mathbb{K} = \int_\Omega \boldsymbol{\nabla}\mathbf{N_x}\boldsymbol{\nabla}\mathbf{N_x^T}\, d\mathbf{x}$$

(4.35)

And also:

$$\begin{cases} \mathbb{M}_{\omega\omega} & = & (\omega\mathbf{N}_\omega, \mathbf{N}_\omega)_{I_\omega} & = & \displaystyle\int_{I_\omega} \mathbf{N}_\omega \omega \mathbf{N}_\omega^T d\omega \\[2em] \mathbb{M}_\omega & = & (\mathbf{N}_\omega, \mathbf{N}_\omega)_{I_\omega} & = & \displaystyle\int_{I_\omega} \mathbf{N}_\omega \mathbf{N}_\omega^T d\omega \\[2em] \mathbf{d} & = & \langle \mathbf{N_x} \cdot \boldsymbol{\delta}, \mathbf{N_x} \rangle_{\Gamma_N} & = & \left[\displaystyle\int_{\Gamma_N} \mathbf{N_x}\mathbf{N_x^T} d\mathbf{x} \right]\{\boldsymbol{\delta}\} \end{cases}$$

(4.36)

where $\boldsymbol{\delta}$ is the discrete form of function $\delta(\mathbf{x} - \mathbf{x_0})$ over Γ_R and $\mathbf{1}$ is a unit vector of the length of the discretization of the parameterized extra-coordinate. Due to all of this, using the tensor PGD notation above introduced, the corresponding discrete system associated to the illustrated model in (4.1) can be rewritten as:

$$\begin{cases} \mathcal{A} & = & \mathbb{A}_1^1 \otimes \mathbb{A}_2^1 + \mathbb{A}_1^2 \otimes \mathbb{A}_2^2 & = & \begin{bmatrix} \mathbf{0} & -\mathbb{M}_x \\ \mathbb{M}_x & \mathbf{0} \end{bmatrix} \otimes \mathbb{M}_{\omega\omega} + \begin{bmatrix} \mathbb{K} & \mathbf{0} \\ \mathbf{0} & \mathbb{K} \end{bmatrix} \otimes \mathbb{M}_\omega \\ \mathcal{B} & = & \mathbf{B}_1^1 \otimes \mathbf{B}_2^1 & = & \mathbf{d} \otimes \mathbf{1} \end{cases}$$

(4.37)

Once the discrete right-hand side and left-hand side terms are finally defined, the approximate representation of the generalized transfer function by a finite

element approach is rightly obtained applying the general framework of PGD above presented. For this reason, it is expected that models being solved using the compact tensor PGD strategy can easily be enhanced, with respect to the inclusion of other thermal properties to the model, just by introducing the corresponding modifications and extra discrete operators into (4.37) in a systematic way.

Chapter 5

Examples of PDG-based real-time monitoring of ATP thermal models

The construction of multi-parametric models for solving the generalized transfer function (3.6) is considered, as proposed in [4, 14]. These enhanced parametric models can incorporate, other than angular frequency, parameters characterizing constitutive behavior besides geometry definition or initial and boundary conditions. Then, by solving the multi-parametric model one time, the solution for any value of the included parameters is made right accessible and thus improved real-time simulation is made possible, as well as inverse analysis and optimization operations.

In what follows, models including anisotropic thermal conductivity and thermal contact conductance as extra-coordinates are implemented into the PGD-based solution of the generalized transfer function which constitutes the off-line stage of the numerical simulation strategy. Then, the obtained models are verified against reference solutions of these models built using finite elements so that real-time monitoring in the on-line stage can be assessed.

Calculations have been carried out using MATLAB® and adapting the existing code developed in the *Institut de Recherche en Génie Civil et Mécanique* at the *École Centrale de Nantes*, to the corresponding requirements.

5.1 Model including anisotropic thermal conductivity

The monitoring strategy proposed in Chapter 3 is applied for building a multi-parametric solution of a model including anisotropic thermal conductivity as extra-coordinate. Parametric analysis of the problem behavior subject to anisotropic

thermal conductivity is of interest since reinforced composite structures, thus not isotropic materials, are produced by the ATP process. First, in the so called off-line stage, problem (4.1) is rewritten with anisotropic thermal conductivity tensor as new parameter, as well as regarding other thermal constants. The space coordinate system is chosen so that it is related to the principal directions of $\boldsymbol{K}$:

$$\boldsymbol{K} = \begin{bmatrix} k_{xx} & k_{xy} \\ k_{yx} & k_{yy} \end{bmatrix} \in \mathbb{R}^2 \quad \rightarrow \quad \boldsymbol{K} = k \cdot \begin{bmatrix} 1 & 0 \\ 0 & \alpha \end{bmatrix} \tag{5.1}$$

where $\alpha = k_{xx}/k_{yy} \in I_k$ is the ratio of the principal thermal conductivities belonging to a predefined range of values. Thus, the influence of relative values of thermal conductivities k_{xx} and k_{yy} with respect to the thermal behavior of the problem can be evaluated by monitoring temperature evolution at for several predefined values of the principal thermal conductivities' ratio. The generalized transfer function is found as the solution to:

$$\begin{cases} im\omega\hat{h} - \boldsymbol{\nabla}\cdot\left(\boldsymbol{K}\cdot\boldsymbol{\nabla}\hat{h}\right) &=& 0 & in\ \Omega \times I_\omega \times I_k \\ \boldsymbol{n}\cdot\left(\boldsymbol{K}\cdot\boldsymbol{\nabla}\hat{h}\right) &=& \delta(\mathbf{x}-\mathbf{x}_0) - l\hat{h} & on\ \Gamma_R \times I_\omega \times I_k \\ \boldsymbol{n}\cdot\left(\boldsymbol{K}\cdot\boldsymbol{\nabla}\hat{h}\right) &=& 0 & on\ \Gamma_N \times I_\omega \times I_k \end{cases} \tag{5.2}$$

which is in turn performed using the associated PDG approximation:

$$\hat{h}(\mathbf{x},\omega,\alpha) \approx \hat{h}^n(\mathbf{x},\omega,\alpha) = \sum_{j=1}^{n} X_j(\mathbf{x}) \cdot W_j(\omega) \cdot K_j(\alpha) \tag{5.3}$$

where $\left\{K_j(\alpha)\right\}_{j=1}^{j=n} \in L^2(I_k)$ are extra separated functions to be determined. The algorithm presented in 4.1 Illustrative example and generalized in 4.2 General framework is applied to determine all functions by implementing the discrete system related to problem (5.2) from equations (4.37), which reads:

$$\begin{cases} \mathcal{A} &=& m\begin{bmatrix} \mathbf{0} & -\mathbb{M}_\mathbf{x} \\ \mathbb{M}_\mathbf{x} & \mathbf{0} \end{bmatrix}\otimes\mathbb{M}_{\omega\omega}\otimes\mathbb{M}_\mathrm{k} + k\begin{bmatrix} \mathbb{K}_{xx} & \mathbf{0} \\ \mathbf{0} & \mathbb{K}_{xx} \end{bmatrix}\otimes\mathbb{M}_\omega\otimes\mathbb{M}_\mathrm{k} \\ && +k\begin{bmatrix} \mathbb{K}_{yy} & \mathbf{0} \\ \mathbf{0} & \mathbb{K}_{yy} \end{bmatrix}\otimes\mathbb{M}_\omega\otimes\mathbb{M}_\mathrm{kk} + l\mathbb{L}\otimes\mathbb{M}_\omega\otimes\mathbb{M}_\mathrm{k} \\ \mathcal{B} &=& \mathbf{d}\otimes\mathbf{1}\otimes\mathbf{1} \end{cases} \tag{5.4}$$

where:

$$\begin{cases}
\mathbb{K}_{xx} & = & \displaystyle\int_{\Omega} \boldsymbol{\nabla}_x(\mathbf{N_x})\boldsymbol{\nabla}_x^T(\mathbf{N_x})\,d\mathbf{x} \\[2em]
\mathbb{K}_{yy} & = & \displaystyle\int_{\Omega} \boldsymbol{\nabla}_y(\mathbf{N_x})\boldsymbol{\nabla}_y^T(\mathbf{N_x})\,d\mathbf{x} \\[2em]
\mathbb{M}_{kk} & = & \displaystyle\int_{I_k} \mathbf{N_k}\alpha\mathbf{N_k}^T d\omega \\[2em]
\mathbb{M}_{k} & = & \displaystyle\int_{I_k} \mathbf{N_k}\mathbf{N_k}^T d\omega \\[2em]
\mathbb{L} & = & \displaystyle\int_{\Gamma_R} \mathbf{N_x}\mathbf{N_x}^T d\mathbf{x}
\end{cases} \qquad (5.5)$$

The tolerance parameter for the alternating directions fixed-point algorithm is set to be the square root of the machine precision, $\varepsilon_e = 10^{-8}$, whilst a maximum number of 50 iterations of the global enrichment procedure are considered. Once the separated representation of $\hat{h}$ is obtained, transient evolution of temperature, $u(\mathbf{x}_0, t_0, \alpha_0)$, from equation (3.8), can be recovered at the monitoring point, $\mathbf{x}_0 \in \Gamma_N$, up to any time instant, $t_0 \in I_t$, and for any predefined value of the ratio of principal thermal conductivities, $\alpha_0 \in I_k$, in what constitutes the on-line stage of the numerical simulation:

$$u(\mathbf{x}_0, t_0, \alpha_0) = u_\infty + \int_0^{t_0} \langle h(\mathbf{x}, \tau, \alpha_0), q(\mathbf{x}, t_0 - \tau)\rangle_{\Gamma_R}\,d\tau \qquad (5.6)$$

The external ambient temperature is rightly added to the obtained solution in the post-process since it is considered to be constant in time. Computer implementation of the problem, besides requiring the use of discrete Fourier transform methods, can take advantage of the separated representation description of the solution of the generalized transfer function when it comes to on-line stage. Taking into account that the external excitation is assumed known beforehand as well as it only depends on space and time coordinates, the singular value decomposition (SVD) technique [15] is applied to approximate a discrete representation of the inflow heat flux:

$$q(\mathbf{x}, t) \approx \sum_{s=1}^{n_q} q_{\mathbf{x}}^s \cdot q_t^s \qquad (5.7)$$

where $q_{\mathbf{x}}$ and q_t are respectively the space and time eigenfunctions of $q(\mathbf{x}, t)$. Consequently, calculation of the transient temperature response turns out to be more compact:

$$u(\mathbf{x}_0, t_0, \alpha_0) \approx \sum_{j=1}^{N} \sum_{s=1}^{n_q} \left(\int_{\Gamma_R} X_j q_{\mathbf{x}}^s \, d\mathbf{x} \cdot \int_{0}^{t_0} T_j q_t^s \, d\tau \cdot K_j \right) \qquad (5.8)$$

where $\{T_j(t)\}_{j=1}^{j=n} \in L^2(I_t)$ are the time modes computed as the inverse Fourier transforms of angular frequency modes resulting from the approximation of the generalized transfer function.

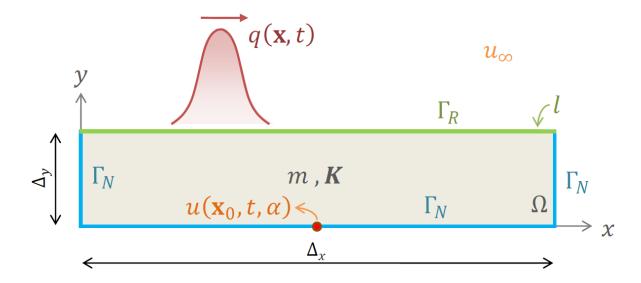### 5.1.1 Problem statement

Figure 5.1   Problem statement

A two-dimensional problem involving a heat flux moving over the upper boundary of a plate domain is considered, whose solution satisfies:

$$\begin{cases} m \dfrac{\partial u}{\partial t} - \boldsymbol{\nabla} \cdot (\boldsymbol{K} \cdot \boldsymbol{\nabla} u) &= 0 & in\ \Omega \times I_t \\ \boldsymbol{n} \cdot (\boldsymbol{K} \cdot \boldsymbol{\nabla} u) &= q - l(u - u_\infty) & on\ \Gamma_R \times I_t \\ \boldsymbol{n} \cdot (\boldsymbol{K} \cdot \boldsymbol{\nabla} u) &= 0 & on\ \Gamma_N \times I_t \\ u &= u_\infty & on\ \Omega \times \{0\} \end{cases} \qquad (5.9)$$

Figure 5.1 depicts the problem statement. Boundary Γ_R is subjected to heat convection while heat transfer is not allowed through Γ_N. The monitoring point is

the midpoint of the bottom boundary. The following constant parameters are considered:

Parameter	Value	Units
Δ_x	1	m
Δ_y	0.2	m
m	1	$J \cdot m^{-3} \cdot K^{-1}$
k	1	$W \cdot m^{-1} \cdot K^{-1}$
l	1	$W \cdot m^{-2} \cdot K^{-1}$
u_∞	298	K

An external thermal source moving from the origin to the right at unit constant velocity along the top surface is modeled from a Gaussian distribution:

$$q(\mathbf{x}, t)|_{\mathbf{x} \in \Gamma_R} = 500 \cdot \exp(-200 \cdot (\mathbf{x} - t)^2) \tag{5.10}$$

expressed in $[W \cdot m^{-2}]$.

A time interval $I_t := (0,1]\ s$ is considered. Regarding the ranges of definition for extra-coordinates, the predefined interval of angular frequencies is $I_\omega := 2\pi \times [-60; 60]\ Hz$, which is wide enough given that there angular frequencies become negligible as their absolute value grows[2]. The range of ratios of the principal thermal conductivities is $I_k := [10^{-2}, 10^2]\ W \cdot m^{-1} \cdot K^{-1}$ and thus the influence of the order of magnitude of the ratio of conductivities in the overall behavior of the solution can be evaluated.

5.1.2 Results

First of all, the generalized transfer function is approximated using PGD. Figure 5.2 shows evolution of the relative residual norm (4.27) with the increase of the number of iterations. The use of the minimal residual PGD scheme is required in order to compute the solution. Thus, 50 terms are necessary to obtain a relative residual of $2 \cdot 10^{-7}$.

---

[2] The analytical expression of the Fourier transform of $q(\mathbf{x}, t)$ is known:

$$\hat{q}(\mathbf{x}, \omega)|_{\mathbf{x} \in \Gamma_R} = 25\sqrt{2\pi} \cdot \exp\left(-\frac{\omega^2}{800}\right) \cdot \exp(-i\omega\mathbf{x})$$

It is noted that the norm of $\hat{q}(\mathbf{x}, \omega)$ is dominated by the term $\exp(-\omega^2/800)$, that ranges from 1 for $\omega = 0$, to 0 as ω approaches infinity. For instance, $\omega = \pm 2\pi \times 60$ the maximum norm of $\hat{q}$ is reduced by a factor of 10^{-78}. Therefore, larger intervals –such as the one above defined– ensure capturing all the significant angular frequency values involved in the calculation of the transform.
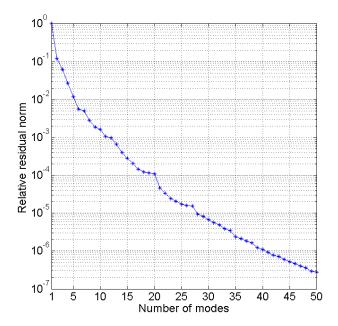
Figure 5.2   Convergence of the generalized transfer function

The first four spatial modes are depicted in Figure 5.3. Discretization of space domain consists of a regular mesh of square elements of side size of 0.02m.

Moreover, first four angular frequency modes are shown in Figure 5.4. The computed implementation considers a non-uniform discretization of I_ω into 501 equally spaced points, refined near zero, where variability of the solution increases.

In addition, modes associated to the ratios of principal thermal conductivities are depicted in Figure 5.5. Since a wide range I_k is considered, the interval is discretized into 5 logarithmically spaced points between 10^{-2} and 10^2.

Verification of the PGD-based approximation of $\hat{h}$ is carried out for some combinations of angular frequencies and ratios of thermal conductivities compared with the corresponding direct solutions obtained by applying the finite element method to (5.2), taking angular frequency and the conductivity tensor as constant parameters. The following pairs of angular frequency and ratio of conductivities, $\{\omega;\ \alpha\}$, are evaluated: $\{-2\pi \times 60;\ 1\}$, $\{0;\ 100\}$ and $\{2\pi \times 60;\ 0.01\}$. The resulting absolute error plots are represented in Figure 5.6.
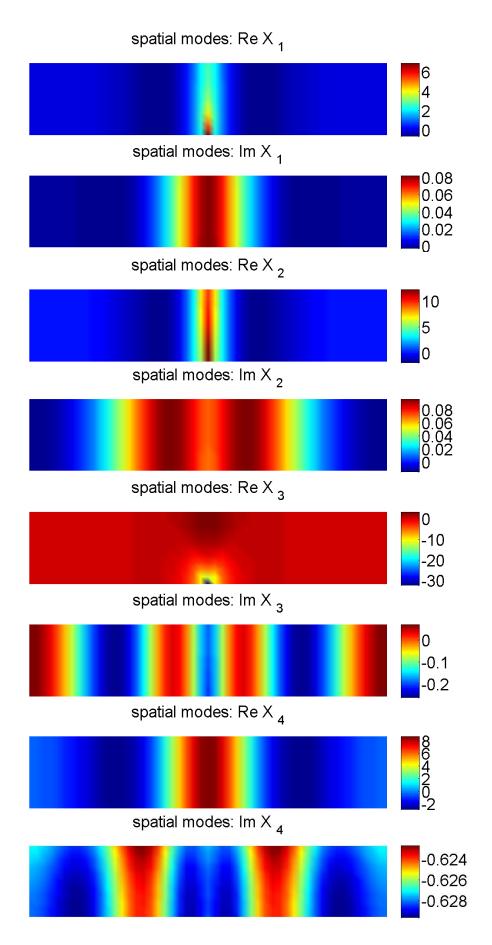
spatial modes: Re X $_1$

spatial modes: Im X $_1$

spatial modes: Re X $_2$

spatial modes: Im X $_2$

spatial modes: Re X $_3$

spatial modes: Im X $_3$

spatial modes: Re X $_4$

spatial modes: Im X $_4$

Figure 5.3 First four spatial real (Re) and imaginary (Im) modes X_1, X_2, X_3 and X_4
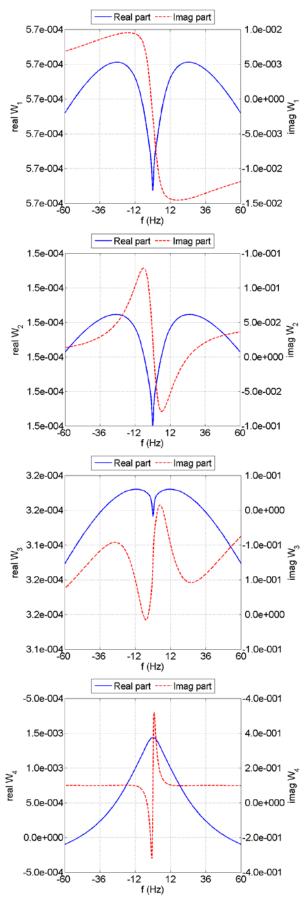
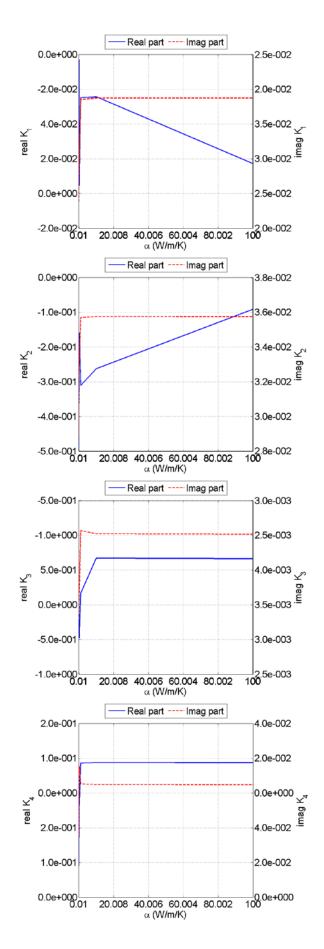Figure 5.4   First four angular frequency modes W_1, W_2, W_3 and W_4

Figure 5.5First four modes of ratio of principal thermal conductivities K_1, K_2, K_3 and K_4
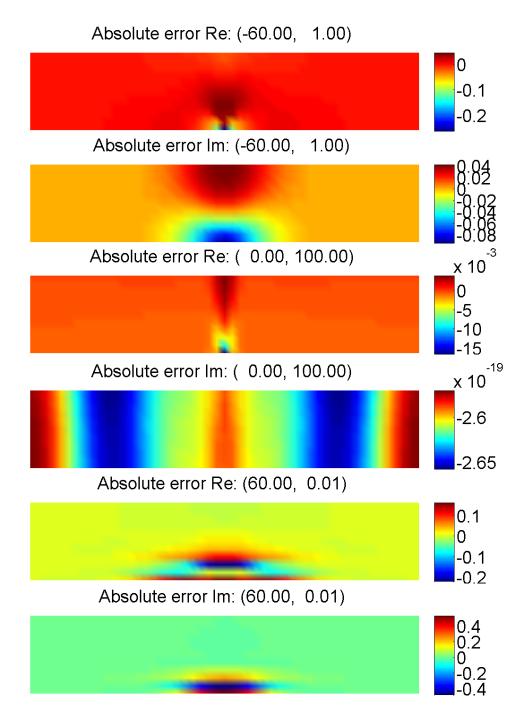
Figure 5.6   Absolute error maps for three $\{\omega;\ \alpha\}$ combinations comparing solutions obtained using PGD and finite elements

Once the generalized transfer function of the problem is obtained in the off-line stage, its inverse Fourier transform can be evaluated and thus computing the convolution integral in equation (5.6) allows for the assessment of on-line temperature monitoring for the given external excitation. This post-process stage is carried out at point $\mathbf{x}_0$ for the time window of interest defined by I_t and for all points in I_k. Verification of the PGD-based solution is conducted against a direct

transient finite element reference solution, using the time-marching scheme presented in the Appendix. Evolution of multi-parametric solutions obtained by the PGD and compared to the reference finite element solution is shown in Figure 5.7.
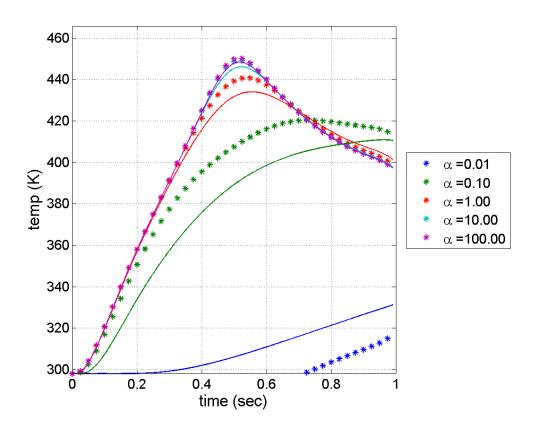

Figure 5.7 Multi-parametric time evolution of temperature at the monitoring point

5.1.3 Discussion

The generalized transfer function being defined as complex-valued, all modes have a real part and imaginary part, as it is shown. When it comes to angular frequency modes, it can also be noted that the real parts are associated to even or symmetric functions whereas imaginary parts correspond to odd or anti-symmetric functions, according to the presented development of the generalized transfer function in Chapter 3.

It is noted that accuracy of the PGD solution is strongly related to the order of magnitude of the ratio of principal thermal conductivities. In the verification of the PGD approximation of the generalized transfer functions for several pairs $\{\omega; \alpha\}$,

31

the solution is observed to get closer to the reference finite element solution as α values increase, which is related to the high variability observed in α modes for small values. Absolute errors of the real and imaginary parts of the depicted maps are of the order of 10^{-3} and 10^{-19} respectively for $\alpha = 10^2$, while absolute error measures for both $\alpha = 10^0$ and $\alpha = 10^{-2}$ are kept around the orders of 10^{-1} and 10^{-2}.

Considering the monitoring results, also a great impact of the order of magnitude of the parameter α is outlined with respect to the behavior of the PGD-based solutions, compared to the reference solutions coming from finite element simulations. Evaluation of the maximum relative error for all parameterized values of the ratio of principal thermal conductivities increases with the decrease of α: for $\alpha = 10^2$, the maximum relative error is 0.09 whereas for $\alpha = 10^{-2}$ the observed measure is 2.69.

Moreover, the influence of the angular frequency interval used in post-processing, in terms of the elapsed time required for the monitoring of the considered time window of 1 second, is noted. Therefore, using the original I_ω from the previous off-line stage, the elapsed time spent for real-time monitoring simulation in a laptop is between 0.03 and 0.10 seconds for all parameter values. If the original angular frequency range is ten times enlarged, as depicted in Figure 5.7, simulation times increase up to 0.13 to 0.15 seconds. However, only slight improvements in the convergence of the proposed solution to the reference one are observed.

5.2 Model including contact thermal conductance

Real-time monitoring of the whole ATP thermal model presented in Chapter 2 is considered herein. Parametric analysis of the impact of introducing an interface subject to a wide range of contact thermal conductance values into the domain in study is relevant to the overall behavior of the solution, since perfect material adhesion of incoming tapes with the welded substrate is not achieved instantaneously during the ATP industrial process. An analogous procedure to the one described for the first model is also applied in this case. A multi-parametric

solution of problem (3.6) is built with contact thermal conductance as an extra parameter besides space and angular frequency domains. General anisotropic thermal conductivity tensor is not included into the separated representation of the generalized transfer function, whose associated PGD approximation reads:

$$\hat{h}(\mathbf{x}, \omega, c) \approx \hat{h}^n(\mathbf{x}, \omega, c) = \sum_{j=1}^{n} X_j(\mathbf{x}) \cdot W_j(\omega) \cdot C_j(c) \qquad (5.11)$$

where $\left\{C_j(c)\right\}_{j=1}^{j=n} \in L^2(I_c)$ are separated functions to be determined within the off-line stage with conductance values within a predefined interval. The discrete system related to problem (3.6) reads:

$$\begin{cases} \mathcal{A} &= m\begin{bmatrix} \mathbf{0} & -\mathbb{M}_{\mathbf{x}} \\ \mathbb{M}_{\mathbf{x}} & \mathbf{0} \end{bmatrix} \otimes \mathbb{M}_{\omega\omega} \otimes \mathbb{M}_c + \begin{bmatrix} \mathbb{K} & \mathbf{0} \\ \mathbf{0} & \mathbb{K} \end{bmatrix} \otimes \mathbb{M}_\omega \otimes \mathbb{M}_c \\ &\quad + l\mathbb{L} \otimes \mathbb{M}_\omega \otimes \mathbb{M}_c + \mathbb{I} \otimes \mathbb{M}_\omega \otimes \mathbb{M}_{cc} \\ \mathcal{B} &= \mathbf{d} \otimes \mathbf{1} \otimes \mathbf{1} \end{cases} \qquad (5.12)$$

where:

$$\begin{cases} \mathbb{K} &= \sum_{s_1=1}^{2} \sum_{s_2=1}^{2} \int_\Omega \boldsymbol{\nabla}_{s_1}(\mathbf{N_x}) k_{s_1 s_2} \boldsymbol{\nabla}_{s_2}^T(\mathbf{N_x}) \, d\mathbf{x} \\[4mm] \mathbb{M}_{cc} &= \int_{I_c} \mathbf{N}_c c \mathbf{N}_c^T dc \\[4mm] \mathbb{M}_c &= \int_{I_c} \mathbf{N}_c \mathbf{N}_c^T dc \\[4mm] \mathbb{I} &= \int_{\Gamma_N^{in}} \mathbf{N_x} \Delta(\mathbf{N_x}^T) d\mathbf{x} \end{cases} \qquad (5.13)$$

Computer implementation of the model with contact thermal conductance duplicates space nodes belonging to Γ_N^{in} so that the temperature drop on the interface can be evaluated. The interior Neumann boundary is split into two contours, $\Gamma_N^{in^+}$ and $\Gamma_N^{in^-}$, with the same geometrical location. Therefore, the discrete operator associated to the spatial modeling of the interface is computed as:

$$\mathbb{I} = \int_{\Gamma_N^{in^+}} \left(\mathbf{N_x^+ N_x^{+^T}} - \mathbf{N_x^+ N_x^{-^T}}\right) d\mathbf{x} + \int_{\Gamma_N^{in^-}} \left(\mathbf{N_x^- N_x^{-^T}} - \mathbf{N_x^- N_x^{+^T}}\right) d\mathbf{x} \qquad (5.14)$$

The on-line post-processing of $\hat{h}$ resulting from the previous stage provides the time evolution of temperature by computing the following convolution integral, given any time instant $t_0 \in I_t$ and any conductance value $c_0 \in I_c$:

$$u(\mathbf{x}_0, t_0, c_0) = u_\infty + \int_0^{t_0} \langle h(\mathbf{x}, \tau, c_0), q(\mathbf{x}, t_0 - \tau) \rangle_{\Gamma_R} \, d\tau \qquad (5.15)$$

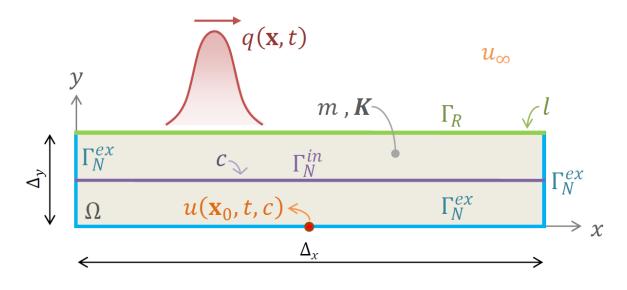### 5.2.1 Problem statement

Figure 5.8   Problem statement

Like in the previous case, a two-dimensional problem involving a heat flux moving over the upper boundary of a plate domain is considered, whose solution satisfies problem (3.6). Figure 5.8 depicts the problem statement. Boundary Γ_R is subjected to heat convection and two Neumann-type boundaries are defined: Γ_N^{ex} the adiabatic exterior boundary and Γ_N^{in}, which is located in the middle height of the rectangular domain, is affected by contact thermal conductance. The monitoring point is the midpoint of the bottom boundary. The following constant parameters are considered:

Parameter	Value	Units
$\mathbf{\Delta_x}$	1	m
$\mathbf{\Delta_y}$	0.2	m
$\boldsymbol{m}$	1	$J \cdot m^{-3} \cdot K^{-1}$
$\boldsymbol{K}$	$\begin{bmatrix} 1 & 0 \\ 0 & 1 \end{bmatrix}$	$W \cdot m^{-1} \cdot K^{-1}$
$\boldsymbol{l}$	1	$W \cdot m^{-2} \cdot K^{-1}$
$\boldsymbol{u_\infty}$	298	K

External thermal source is considered to be the one already defined for the previous problem. Moreover, the intervals of definition for time and angular frequency are maintained. The range of contact thermal conductances is $I_c := [10^{-2}, 10^2] \, W \cdot m^{-2} \cdot K^{-1}$ so that the influence of the order of magnitude of c in the overall behavior of the solution can be analyzed.

5.2.2 Results

Figure 5.9 shows evolution of the relative residual norm (4.27) with the increase of the number of iterations. The use of the minimal residual PGD scheme is required again in order to compute the solution. 50 global enrichment steps are necessary to reach a relative residual of $4.0 \cdot 10^{-7}$.
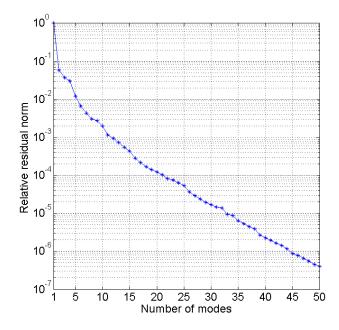

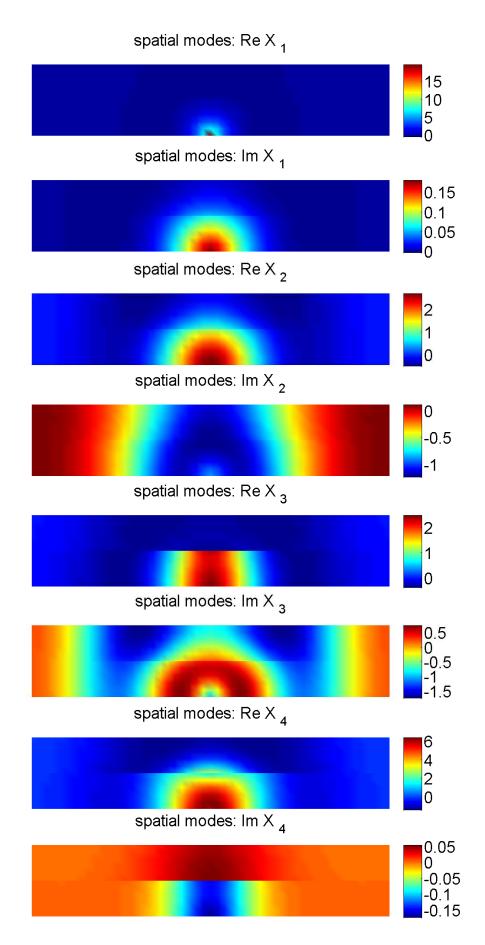Figure 5.9   Convergence of the generalized transfer function

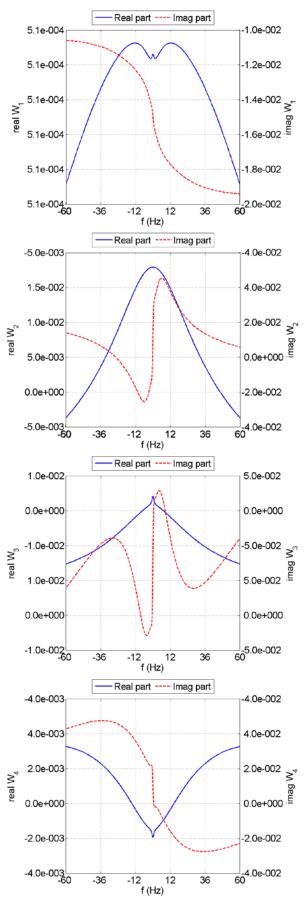Figure 5.10First four spatial real (Re) and imaginary (Im) modes X_1, X_2, X_3 and X_4

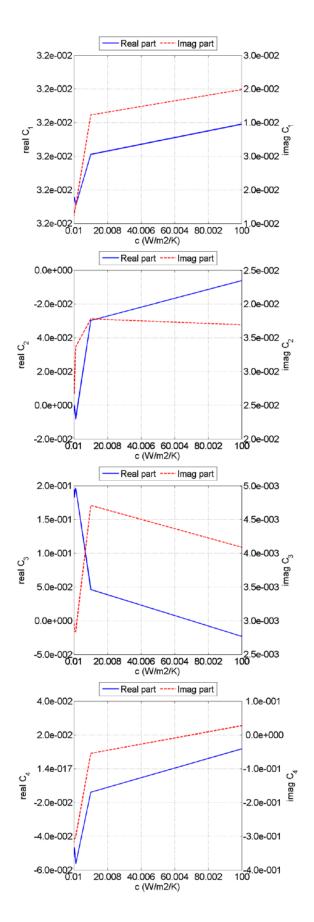Figure 5.11   First four angular frequency modes W_1, W_2, W_3 and W_4

Figure 5.12   First four modes of ratio of principal thermal conductivities C_1, C_2, C_3 and C_4
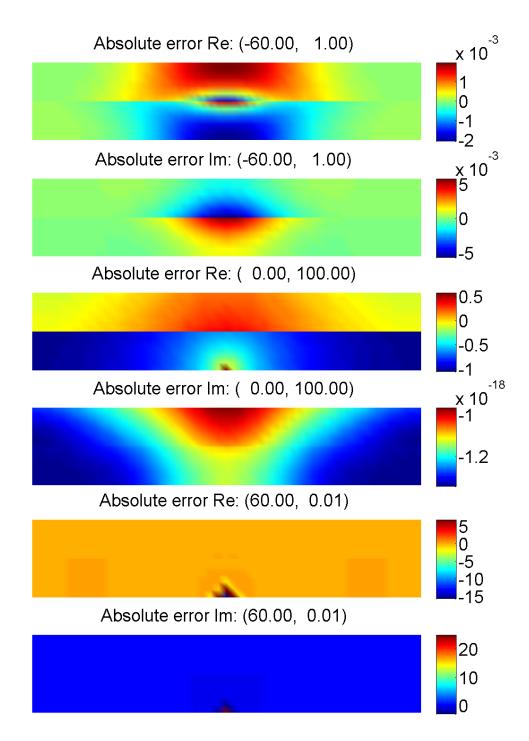
Figure 5.13   Absolute error maps for three $\{\omega; \ c\}$ combinations comparing solutions obtained using PGD and finite elements

The first four spatial modes are depicted in Figure 5.10. Discretization of space domain consists of a regular mesh of square elements of side size of 0.02m.

Also, first four angular frequency modes are shown in Figure 5.11. I_ω is again discretized into 501 equally spaced points, refined near zero, where variability of the solution increases.

Moreover, modes associated to contact thermal conductances are depicted in Figure 5.12. Since a wide range I_c is considered, the interval is discretized into 5 logarithmically spaced points between 10^{-2} and 10^2.

Verification of the PGD-based approximation of $\hat{h}$ is performed for the following pairs of $\{\omega; c\}$: $\{-2\pi \times 60; 1\}$, $\{0; 100\}$ and $\{2\pi \times 60; 0.01\}$. Reference solutions are obtained by applying the finite element method to (3.6), taking constant angular frequency and the contact thermal conductance. The resulting absolute error plots are represented in Figure 5.13.

The on-line temperature monitoring from equation (5.15) is carried out at point $\mathbf{x}_0$ for the time window of interest defined by I_t and for all points in I_c. Verification of the PGD-based solution is conducted against a direct transient finite element reference solution, using again the time-marching scheme presented in the Appendix. Evolution of multi-parametric solutions resulting from application of the PGD, compared to the reference finite element solution is shown in Figure 5.14.
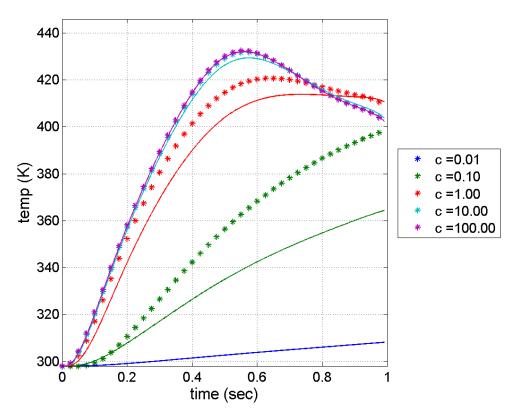

Figure 5.14   Multi-parametric time evolution of temperature at the monitoring point

5.2.3 Discussion

The same kind of analysis of results can be conducted for the current problem. Real and imaginary parts arise from calculation by definition of the problem in study. Accuracy of the PGD solution is again strongly related to the order of magnitude of the contact thermal resistance parameter, since the obtained solutions are observed to get closer to the reference finite element solution for moderate c values, which is related to the high variability of c modes for extreme range values. Absolute errors of the real and imaginary parts of the depicted maps are of the order of 10^{-3} for $c = 10^0$, while absolute error measures for $c = 10^{-2}$ and $c = 10^2$ are increased up to the orders of 10^1 and 10^0 respectively.

Also a great impact of the order of magnitude of the parameter c is outlined with respect to the behavior of monitoring based on the PGD-based solutions, compared to the reference direct solutions coming from finite element simulations. Maximum relative error turns out to be inversely proportional to the value of parameterized contact conductances: for $c = 10^2$, the maximum relative error is of the order of 0.01 whereas for $\alpha = 10^{-2}$ the observed measure is of the order of 5.57.

Finally, the influence of angular frequencies interval used in post-processing is noted. Using the original I_ω from the previous off-line stage, the elapsed time spent for real-time monitoring simulation of 1 second in a laptop remains between 0.03 and 0.10 seconds for all parameter values. If the original angular frequency range is ten times enlarged, as depicted in Figure 5.14, simulation times increase up to 0.14 to 0.17 seconds, entailing negligible improvements in the convergence of the proposed solution to the reference finite element solution.

In view of the above results, the proposed numerical simulation strategy for real-time temperature monitoring based on multi-parametric PGD-based solutions, including the ratio of principal conductivities of the problem as well as contact thermal conductance as extra-coordinates, is confirmed to be a fast methodology with performance levels strongly dependent on the problem scaling. Convergence of the proposed solution to reference solutions obtained using robust techniques is satisfied for the higher order parameter values of the predefined ranges.

Therefore, the adjustment of all thermal properties of problems to be solved using PGD can provide useful virtual charts for practical applications.

Chapter 6

Conclusions

ATP real-time thermal monitoring using numerical simulations has been assessed in this work. The off-line stage of the proposed methodology has been studied by computing PGD-based multi-parametrical solutions of the generalized transfer functions associated to two problems, one model including anisotropic thermal conductivity as extra-coordinate and also a model including an interface subject to contact thermal conductance. Then, fast on-line calculations of transient temperature field have been carried out.

Computer implementation of the aforementioned problems has evidenced that the accuracy of solutions obtained by the PGD separated representation approach are strongly dependent on the order of magnitude of the ranges of considered extra-coordinates. Although good results have been observed for certain values of the extra parameters, compared to reference solutions by finite element schemes, it is noted that problem scaling needs to be adjusted beforehand when building up virtual charts of solutions for multi-parametric models regarding wide ranges of definition. Therefore, validation of the proposed monitoring strategy against experimental data is required in order to construct numerical useful solutions with practical applicability.

Further research lines in the study of real-time monitoring of the ATP process may take into account:

- Construction of multi-parametric PGD solutions including more thermal parameters, such as heat transfer coefficient on the substrate-placement head interface.
- Optimization of codes so that off-line PGD high-dimensional separated representation of solutions can be achieved with reasonable computational

costs, and convergence of the fixed point algorithm do not require using expensive methodologies such as the symmetrized PGD for the thermal model in study.

- Addition of more complex phenomena to the ATP thermal model, and thus enriched numerical simulations, considering the effect of bonding kinetics or void growth to the overall behavior of the problem.

- Application of enhanced off-line multi-parametric solutions of the generalized transfer function to inverse identification problems, in order to conduct on-line calibration of the imposed external excitation with respect to the amplitude or speed of the inflow heat flux.

Appendix

Full finite element reference solutions

The finite element (FE) method is used in this work as the verification tool to establish reference solutions to compare the proposed PGD-based computations to. As discussed in 4.3 Computer implementation, the application of finite element discretizations when computing the separated representation of unknown fields can take advantage of using the same technique for the assessment operations, as the whole numerical strategy is optimized since the discrete form of involved operators can be evaluated just one time. Moreover, parametric analyses are precluded when using FE and thus direct, yet robust, solutions have to be recomputed for all desired combinations of parameters. The finite element approach for solving the generalized transfer function assuming all parameters known, as well as the transient temperature response or the full thermal problem associated to the ATP process are presented in this Appendix.

First, the solution of the generalized transfer function (3.6) is considered. The associated weak formulation reads:

Find $\hat{h}(\boldsymbol{x}) \in H^1(\Omega)$ such that

$$\left(im\omega\hat{h}, \hat{v}\right)_\Omega + \left(\boldsymbol{K} \cdot \boldsymbol{\nabla}\hat{h}, \boldsymbol{\nabla}\hat{v}\right)_\Omega + \langle l\hat{h}, \hat{v}\rangle_{\Gamma_R} + \langle c\Delta\hat{h}, \hat{v}\rangle_{\Gamma_N^{in}} = \hat{v}^*(\mathbf{x}_0) \qquad (\text{A.1})$$

for all test function $\hat{v} \in H^1(\Omega)$

Since $\hat{h}(\mathbf{x})$ is a complex-valued field, its solution is decomposed into the corresponding real and imaginary parts, namely:

$$\hat{h}(\mathbf{x}) = \text{Re}(\hat{h}) + i\,\text{Im}(\hat{h}) \in \mathbb{C} \qquad (\text{A.2})$$

Vector $\mathbf{N_x}$ containing the discrete shape functions for interpolation over the space domain is recalled. The following matrices of the discrete form of involved operators are defined recalling the notation used in 4.3 Computer implementation and 5.1 Model including anisotropic thermal conductivity and 5.2 Model including contact thermal conductance:

$$\begin{cases} \mathbb{M} & = & (m\omega\mathbf{N_x},\mathbf{N_x})_\Omega & = & m\omega \int_\Omega \mathbf{N_x}\mathbf{N_x}^T d\mathbf{x} \\[2em] \mathbb{K} & = & (\boldsymbol{K}\cdot\boldsymbol{\nabla}\mathbf{N_x},\boldsymbol{\nabla}\mathbf{N_x})_\Omega & = & \int_\Omega \boldsymbol{\nabla}\mathbf{N_x}\cdot\boldsymbol{K}\cdot\boldsymbol{\nabla}\mathbf{N_x}^T d\mathbf{x} \\[2em] \mathbb{L} & = & (l\mathbf{N_x},\mathbf{N_x})_{\Gamma_R} & = & l \int_{\Gamma_R} \mathbf{N_x}\mathbf{N_x}^T d\mathbf{x} \\[2em] \mathbb{I} & = & (c\Delta(\mathbf{N_x}),\mathbf{N_x})_{\Gamma_N^{in}} & = & c \int_{\Gamma_N^{in}} \mathbf{N_x}\Delta(\mathbf{N_x}^T) d\mathbf{x} \end{cases} \qquad (\text{A.3})$$

Computation of the matrix modeling the interface is performed following equation (5.14), which considers the duplication of nodes belonging to the interior Neumann boundary of the domain. Therefore, for each combination of thermal parameters, the solution of the generalized transfer function is found by solving the following system:

$$\begin{bmatrix} \mathbb{K}+\mathbb{L}+\mathbb{I} & -\mathbb{M} \\ \mathbb{M} & \mathbb{K}+\mathbb{L}+\mathbb{I} \end{bmatrix} \begin{Bmatrix} \hat{\mathbf{h}}_{Re} \\ \hat{\mathbf{h}}_{Im} \end{Bmatrix} = \begin{Bmatrix} \mathbf{d} \\ \mathbf{0} \end{Bmatrix} \qquad (\text{A.4})$$

where $\hat{\mathbf{h}}_{Re}$ and $\hat{\mathbf{h}}_{Im}$ are the discrete counterparts of the complex decomposition of $\hat{h}$ and vector $\mathbf{d}$ is the known discrete form of function $\delta(\mathbf{x}-\mathbf{x}_0)$ over Γ_R.

Second, the solution of the temperature field associated to transient problem (2.1) is considered. The associated weak formulation reads:

Find $u \in H^1(\Omega)$ such that $u(\boldsymbol{x},0)=u_\infty$ and

$$(mu,v)_\Omega + (\boldsymbol{K}\cdot\boldsymbol{\nabla}u,\boldsymbol{\nabla}v)_\Omega + \langle lu,v \rangle_{\Gamma_R} + \langle c\Delta u,v \rangle_{\Gamma_N^{in}} = \langle q,v \rangle_{\Gamma_R} \qquad (\text{A.5})$$

for all test function $\hat{v} \in H^1(\Omega)$

Time evolution of temperature on the space domain is computed applying a so-called θ-family method [16] for discrete time integration of initial value problems. First of all, the time window is subdivided into discrete steps, $\{\Delta t^j\}_{j=1}^{j=N}$. Then, starting from the imposed initial solution, the time-marching scheme updates each new space domain solution from already calculated solutions. The solution update for two successive time steps t^n and t^{n+1} considering a weighting parameter $\theta \in [0;1]$ reads:

$$[\mathbb{M} + \theta \Delta t^n (\mathbb{K} + \mathbb{L} + \mathbb{I})]\mathbf{u}^{n+1} - \theta \Delta t^n \mathbf{q}^{n+1}$$
$$= (1 - \theta)\Delta t^n \mathbf{q}^n + [\mathbb{M} - (1 - \theta)\Delta t^n (\mathbb{K} + \mathbb{L} + \mathbb{I})]\mathbf{u}^n \qquad (\text{A.6})$$

where $\mathbf{u}^n$ and $\mathbf{u}^{n+1}$ are the successive updates of the temperature field and vectors $\mathbf{q}^n$ and $\mathbf{q}^{n+1}$ are the known discrete forms of the external excitation $q(\mathbf{x}, t)$ acting on Γ_R at two consecutive time instants. In this work, the Crank-Nicholson method of time integration is used, that is the θ-family method with $\theta = \frac{1}{2}$, because of this implicit method being unconditionally stable and having a quadratic convergence with respect to the time step size. Equation (A.6) is simplified in this case, reading:

$$\left[\mathbb{M} + \frac{\Delta t^n}{2}(\mathbb{K} + \mathbb{L} + \mathbb{I})\right]\mathbf{u}^{n+1} = \left[\mathbb{M} - \frac{\Delta t^n}{2}(\mathbb{K} + \mathbb{L} + \mathbb{I})\right]\mathbf{u}^n + \frac{\Delta t^n}{2}(\mathbf{q}^n + \mathbf{q}^{n+1}) \qquad (\text{A.7})$$

As a final remark, problem cases not including contact thermal conductance in interface boundaries, such as 5.1 Model including anisotropic thermal conductivity, can be solved using the same FE-based approaches above described without adding the discrete operator associated to this boundary condition to the corresponding systems and neither duplicating nodes of the spatial domain mesh.

Reference list

[1]   Chinesta, F.; Leygue, A.; Bognet, B.; Ghnatios, Ch.; Poulhaon, F.; Bordeu, F.; Barasinski, A.; Poitou, A.; Chatel, S. and Maison-Le-Poec, S. First steps towards an advanced simulation of composites manufacturing by automated tape placement. *Int. J. Mater. Form.* 2014, 7: 81–92.

[2]   Stokes-Griffin, C.M.; Matuszyk, T.I.; Compston, P. and Cardew-Hall, M.J. Modelling the Automated Tape Placement of Thermoplastic Composites with In-Situ Consolidation. *Sustainable Automotive Technologies 2012* 2012, 61–68.

[3]   Chinesta, F.; Ladeveze, P. and Cueto, E. A Short Review on Model Order Reduction Based on Proper Generalized Decomposition. *Arch. Comput. Methods Eng.* 2011, 18: 395–404.

[4]   Aguado, J.V.; Huerta, A.; Chinesta, F. and Cueto, E. Real-time monitoring of thermal processes by reduced order modeling. Submitted, 2014.

[5]   Nicodeau, C.; Regnier, G.; Verdu, J.; Chinesta, F. and Cinquin, J. Une approche multi-physique du soudage en continu des composites à matrice thermoplastique: vers une modélisation multi-échelle. 18ème CFM, Grénoble 2007. <http://documents.irevues.inist.fr/handle/2042/15971> (accessed July 4, 2014).

[6]   Weisstein, Eric W. "Fourier Transform." From MathWorld--A Wolfram Web Resource.   <http://mathworld.wolfram.com/FourierTransform.html> (accessed July 4, 2014).

[7]   Chopra, A. K. Appendix A. Frequency-Domain Method of Response Analysis. In: *Dynamics of structures: Theory and Applications to Earthquake Engineering*. 4th ed. Prentice-Hall 2011, 883–904.

[8]   Chinesta, F.; Leygue, A.; Bordeu, F.; Aguado, J.V.; Cueto, E.; Gonzalez, D.; Alfaro, I.; Ammar, A. and Huerta, A. PGD-Based Computational Vademecum for Efficient Design, Optimization and Control. *Arch. Comput. Methods Eng.* 2013, 20(1): 31–59.

[9]   Chinesta, F.; Ammar, A. and Cueto, E. Recent Advances and New Challenges in the Use of the Proper Generalized Decomposition for Solving Multidimensional Models. *Arch. Comput. Methods Eng.* 2010, 17: 327–350.

[10]   Ammar, A.; Normandin, M.; Daim, F.; Gonzalez, D.; Cueto, E. and Chinesta, F. Non incremental strategies based on separated representations: applications in computational rheology. *Commun. Math. Sci.* 2010, 8(3): 671–695.

[11]   Ammar, A; Chinesta, F.; Diez, P. and Huerta, A. An error estimator for separated representations of highly multidimensional models. *Computer Methods in Applied Mechanics and Engineering* 2010, 199: 1872–1880.

[12]   Falcó, A. and Nouy, A. A Proper Generalized Decomposition for the solution of elliptic problems in abstract form by using a functional Eckart-Young approach. *J. Math. Anal. Appl.* 2011, 376: 469–480.

[13]   Lozinski, A. Interplay between PGD and greedy approximation algorithms for high-dimensional PDEs: Symetric and not symetric cases. Journées Scientifiques CSMA 2010. <http://website.ec-nantes.fr/reduc/Programme/Pr%E9sentation/session_4_lozinski.pdf> (accessed July 4, 2014).

[14]   Prulière, E.; Chinesta, F.; Ammarc, A.; Leygue, A. and Poitou, A. On the solution of the heat equation in very thin tapes. *International Journal of Thermal Sciences* 2013, 65: 148–157.

[15]   Shlens, J. A Tutorial on Principal Component Analysis. *arXiv:1404.1100v1 [cs.LG]*, Apr 3, 2014. <http://arxiv.org/pdf/1404.1100v1.pdf> (accessed July 4, 2014).

[16]   Universitat Politècnica de Catalunya, BarcelonaTech. *Finite element solution of transient convection-diffusion problems*. Lecture notes distributed in Computational engineering on spring 2013.